

# Understanding the Origins of Higher Capacities at Faster Rates in Lithium-Excess $\text{Li}_x\text{Ni}_{2-4x/3}\text{Sb}_{x/3}\text{O}_2$

Nancy Twu,<sup>†</sup> Michael Metzger,<sup>‡</sup> Mahalingam Balasubramanian,<sup>¶</sup> Cyril Marino,<sup>§</sup> Xin Li,<sup>||</sup> Hailong Chen,<sup>⊥</sup> Hubert Gasteiger,<sup>‡</sup> and Gerbrand Ceder<sup>\*,#</sup>

<sup>†</sup>Department of Materials Science and Engineering, Massachusetts Institute of Technology, Cambridge, Massachusetts 02139, United States

<sup>‡</sup>Chair of Technical Electrochemistry, Technische Universität München, 85748 Garching, Germany

<sup>¶</sup>X-ray Science Division, Advanced Photon Source, Argonne National Laboratory, Argonne, Illinois 60439, United States

<sup>§</sup>Paul Scherrer Institut, 5232 Villigen PSI, Switzerland

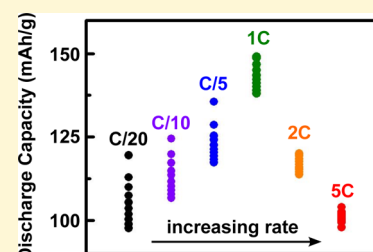
<sup>||</sup>School of Engineering and Applied Sciences, Harvard University, Cambridge, Massachusetts 02138, United States

<sup>⊥</sup>The Woodruff School of Mechanical Engineering, Georgia Institute of Technology, Atlanta, Georgia 30332, United States

<sup>#</sup>Department of Materials Science and Engineering, University of California, Berkeley, California 94720, United States

## Supporting Information

**ABSTRACT:** The lithium-excess  $\text{Li}_x\text{Ni}_{2-4x/3}\text{Sb}_{x/3}\text{O}_2$  (LNSO) materials were previously shown to demonstrate higher capacities and improved cyclability with increasing lithium content. While the performance trend is promising, observed capacities are much lower than theoretical capacities, pointing to a need for further understanding of active redox processes in these materials. In this work, we study the electrochemical behavior of the LNSO materials as a function of lithium content and at slow and fast rates. Surprisingly,  $\text{Li}_{1.15}\text{Ni}_{0.47}\text{Sb}_{0.38}\text{O}_2$  (LNSO-15) exhibits higher discharge capacities at faster rates and traverses distinct voltage curves at slow and fast rates. To understand these two peculiarities, we characterize the redox activity of nickel, antimony, and oxygen at different rates. While experiments confirm some nickel redox activity and oxygen loss, these two mechanisms cannot account for all observed capacity. We propose that the balance of the observed capacity may be due to reversible oxygen redox and that the rate-dependent voltage curve features may derive from irreversible nickel migration occurring on slow charge. As future high energy density cathodes are likely to contain both lithium excess and high nickel content, both of these findings have important implications for the development of novel high capacity cathode materials.



## INTRODUCTION

One of the major bottlenecks to higher energy density lithium-ion batteries is developing higher capacity cathode materials.<sup>1</sup> To date, the highest reversible capacities in lithium-ion chemistries have been achieved in lithium-excess transition metal oxides.<sup>2–6</sup> While these materials have long been of interest given their high cycling capacities, they still require improvement in rate capability,<sup>7–11</sup> as well as elucidation of the first charge activation processes and their consequences.<sup>5,12–14</sup>

Recently, lithium excess was proposed by Lee and co-workers<sup>3,15</sup> as a means of enhancing lithium diffusion through percolation of low barrier lithium diffusion channels. This design strategy was applied to the layered lithium-excess  $\text{Li}_x\text{Ni}_{2-4x/3}\text{Sb}_{x/3}\text{O}_2$  (LNSO) materials, recently reported as a new family of cathode materials.<sup>16</sup> The lithium-excess LNSO materials show greatly improved discharge capacity and cyclability over their stoichiometric counterpart. However, despite being an exciting proof-of-concept, the experimental capacities of the LNSO materials are far below their theoretical capacities and require further understanding of which phenomena limit capacity.

In this paper, we study the redox mechanisms of four lithium-excess LNSO materials with 0–15% lithium excess as a function of lithium content and rate. Hereafter, we refer to these materials as LNSO-*n*, where *n* represents the amount of excess lithium. We show that an oxygen loss plateau emerges with increasing lithium content, similar to other lithium-excess layered oxides. More interestingly, at the highest lithium-excess level,  $\text{Li}_{1.15}\text{Ni}_{0.47}\text{Sb}_{0.38}\text{O}_2$  (LNSO-15), the oxygen loss plateau disappears with increased charge rate, and we observe *higher discharge capacities at faster rates*. From careful characterization of nickel, antimony, and oxygen redox activity, we determine which redox processes are active at slow and fast rates and propose nickel migration may explain the anomalous rate behavior.

Special Issue: Computational Design of Functional Materials

Received: November 2, 2016

Revised: February 6, 2017

Published: February 8, 2017

## EXPERIMENTAL SECTION

The LNSO materials were synthesized by solid state reaction, details of which are previously described.<sup>16</sup> The weight percents of Li, Ni, and Sb in LNSO-5, LNSO-10, and LNSO-15 compositions were determined using ICP-AES with bomb digestion (25% RSD) by Micro-Analysis, Inc. and converted to atomic percents in the Supporting Information. After synthesis at 800–900 °C, the active material was mixed with carbon black in a planetary ball mill to achieve a final particle size of 500–100 nm. Self-standing electrode films were made with LNSO, carbon, and polytetrafluoroethylene (PTFE) binder in a ratio of 80:15:5 by weight. Swagelok cells for galvanostatic cycling and galvanostatic intermittent titration technique (GITT) measurements were assembled in an argon-filled glovebox using a 5/16 in. diameter LNSO film as the cathode (active material loading of 2.6–4.4 mg/cm<sup>2</sup>), Li metal as the anode, Celgard 2320 as separator, and 1 M LiPF<sub>6</sub> in EC/DMC as electrolyte. Cells were cycled on a Maccor 2200 or Maccor 4000 operating at room temperature. For the GITT measurement, a C/20 current pulse was applied for 30 min followed by an OCV step of 10 h.

Charged and cycled cells for *ex situ* measurements were disassembled in a glovebox to minimize air exposure. Samples for electron energy loss spectroscopy (EELS) and high resolution transmission electron microscopy (HRTEM) were lightly sonicated in DMC in a glovebox to disperse the cathode film into small particles; EELS spectra and HRTEM images were then collected on a JEOL 2010F. Cathode films for *ex situ* X-ray absorption near edge structure (XANES) were taped between two pieces of Kapton tape in a glovebox. XANES spectra were collected in transmission mode at the Argonne National Laboratory Advanced Photon Source, beamline 20-BM-B.

*In situ* X-ray diffraction (XRD) patterns were obtained in 40 min intervals from a laboratory Bruker D8 Advance Da Vinci Mo-source diffractometer scanned between 8 and 30° 2θ and then converted to a 2θ range corresponding to a Cu source. The *in situ* cell contains a beryllium window for X-ray penetration and was configured similar to Swagelok cells but with glass fiber as separator. The cell was cycled in galvanostatic mode on a Solatron SI12287 in the voltage window of 2.5–4.6 V at a current rate of C/20. Rietveld refinement on the XRD patterns was completed using PANalytical High Score Plus for every other scan. In general, electrodes with higher active material loading were required for the *ex situ* and *in situ* measurements. Unfortunately, higher active material loading corresponds to thicker self-standing films, which tends to compromise cycling performance and results in lower capacities at high rates.

*In situ* gas analysis by online electrochemical mass spectroscopy (OEMS) was performed for LNSO-15/Li metal and LNSO-0/Li metal half-cells. Working electrodes for OEMS testing were punched to a diameter of 15 mm, with active material loadings of 3.9 mg/cm<sup>2</sup> for LNSO-15 and 5.0 mg/cm<sup>2</sup> for LNSO-0. The OEMS test cells were assembled in custom cell hardware<sup>17,18</sup> using a metallic lithium counter electrode, two glass fiber separators, and 1 M LiPF<sub>6</sub> in EC/DMC as electrolyte. The OEMS setup can detect ppm level gas constituents<sup>19</sup> and is previously described in detail.<sup>17</sup> The gas evolution during charge was measured at 25 °C, with cells first held at OCV for 2 h and then galvanostatically charged at a rate of C/20 to a cutoff potential of 4.6 V. Conversion of the mass spectrometer currents to concentrations was done for oxygen, carbon dioxide, and carbon monoxide using a calibration gas (H<sub>2</sub>, O<sub>2</sub>, CO, and CO<sub>2</sub> at 2000 ppm each in argon).

## RESULTS

**Electrochemical Performance.** The voltage versus specific capacity plots for the four LNSO compounds cycled at C/20 are shown in Figure 1a, in order of increasing lithium content from top to bottom. Although the LNSO compounds have different theoretical capacities (Table 1), the plots are stacked vertically on the same x-axis to visually highlight trends in first charge, capacity retention, and discharge voltage profiles with lithium excess. For LNSO-0 and LNSO-5, the theoretical capacity is calculated on the basis of complete Li removal, while for LNSO-10 and LNSO-15, the theoretical capacity is set by the Ni<sup>2+/4+</sup> redox couple.

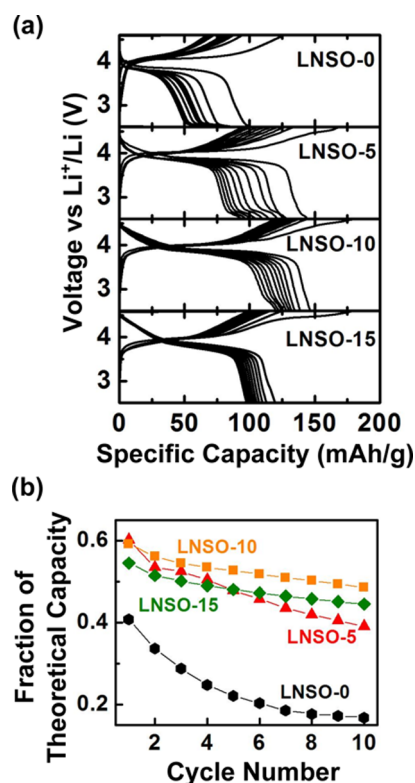


**Figure 1.** (a) From top: Galvanostatic cycling of LNSO-0, LNSO-5, LNSO-10, and LNSO-15 at C/20 between 2.5 and 4.6 V. (b) Fraction of theoretical capacity achieved on discharge over ten cycles at C/20 between 2.5 and 4.6 V. Capacity retention improves with increasing lithium content, and all lithium-excess samples access a higher fraction of their theoretical capacities than LNSO-0.

**Table 1.** Theoretical Capacities of Li<sub>x</sub>Ni<sub>2-4x/3</sub>Sb<sub>x/3</sub>O<sub>2</sub> Compounds Calculated from the Ni<sup>2+/4+</sup> Redox Couple

sample	formula	theoretical capacity (mAh/g)
LNSO-0	Li <sub>1.00</sub> Ni <sub>0.67</sub> Sb <sub>0.33</sub> O <sub>2</sub>	226
LNSO-5	Li <sub>1.05</sub> Ni <sub>0.60</sub> Sb <sub>0.35</sub> O <sub>2</sub>	240
LNSO-10	Li <sub>1.10</sub> Ni <sub>0.53</sub> Sb <sub>0.37</sub> O <sub>2</sub>	247
LNSO-15	Li <sub>1.15</sub> Ni <sub>0.47</sub> Sb <sub>0.38</sub> O <sub>2</sub>	219

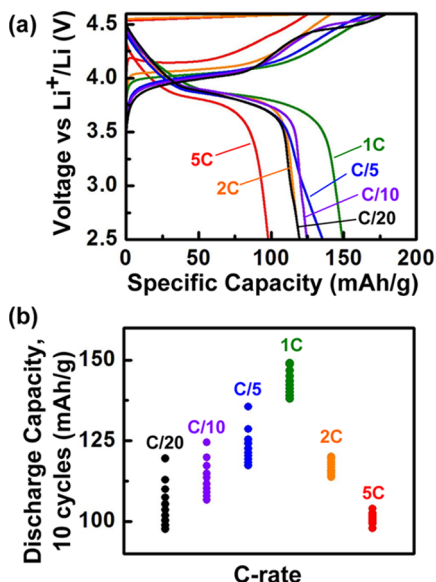
The first charge of LNSO-0 shows a single plateau at 4 V, while the first charge of the lithium-excess LNSO compounds shows a plateau at 4 V and one at 4.45 V. The 4 V plateau accounts for approximately half the theoretical Ni<sup>2+/4+</sup> redox capacity of each compound, and the length of the 4.45 V plateau increases with increasing lithium content. Charge capacity obtained along the 4.45 V plateau is absent in discharge.

Figure 1b shows the C/20 discharge capacities plotted as a function of cycle number. Because each LNSO compound has a different theoretical capacity, the discharge capacity is normalized by dividing the experimental discharge capacity by the theoretical capacity. Compared to LNSO-0, the lithium-excess LNSO compounds show two noticeable improvements. First, the fraction of theoretical capacity accessed on discharge by all the lithium-excess LNSO compounds is much higher. Second, increasing lithium content reduces capacity fade.

One final feature in Figure 1a to note is the small voltage step at 2.6 V on discharge. The LNSO-0, LNSO-5, and LNSO-10 compounds show this 2.6 V step to evolve over ten cycles, becoming most pronounced in the tenth cycle. The 2.6 V

feature is less pronounced with increasing lithium content and is not observed at all in the LNSO-15 voltage curves. At present, we do not know what phenomena are responsible for this voltage step.

We find that, at faster rates, the LNSO compounds containing 0–10% lithium excess exhibit typical rate behavior: higher C-rates lead to lower capacities and increased polarization. In contrast, LNSO-15 shows the opposite, highly unexpected behavior between C/20 and 1C and is demonstrated in Figure 2.



**Figure 2.** (a) First cycle voltage curves of LNSO-15 obtained from galvanostatic cycling between C/20 and 5C. At faster C-rates, the 4.45 V charge plateau disappears, and higher discharge capacities are achieved. (b) Discharge capacity over ten cycles for LNSO-15 at rates

Upon charge, all cells between C/20 and 1C reach approximately the same final charge capacity but with increasing rate leading to a deferral of the 4.45 V plateau. Upon discharge, as the rate increases from C/20 to 1C, the discharge capacity increases. This increase in discharge capacity increases the first-cycle Coulombic efficiency between C/20 and 1C. Only when the rate is increased to 2C and 5C do both charge and discharge capacity decrease, which is likely due to traditional polarization effects. For the cells tested at 2C and 5C, we observe that the charge voltage is increased and the discharge voltage is depressed. The first cycle voltage curves for LNSO-15 obtained at C/20, C/10, C/5, 1C, 2C, and 5C are overlaid in Figure 2a. The C-rate dependence of the discharge capacity is summarized in Figure 2b. Pristine cells are used for each rate test.

The anomalous rate behavior of LNSO-15 motivates the remainder of this work. First, we conducted additional electrochemical tests to characterize the 4.45 V plateau and understand its relationship to reversible capacity. Second, using a range of characterization techniques, we determine which redox processes are active at fast and slow rates.

**Characterization of the 4.45 V Plateau.** Rate tests on LNSO-15 suggest that the processes occurring along the 4.45 V plateau are slow, as this plateau disappears upon higher C-rates. This observation is further supported by galvanostatic intermittent titration technique (GITT) measurements, shown in Figure 3. Small overpotentials are observed along the first 4 V plateau, indicating a faster process, and larger overpotentials are

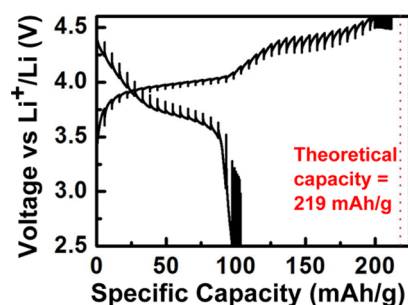


**Figure 3.** GITT measurements on LNSO-15 show a low overpotential along the first charge plateau and a larger overpotential along the second charge plateau. The 4.45 V overpotential of the second plateau agrees well with voltage curves obtained by galvanostatic cycling. The

observed along the second plateau, indicating a slower process. The overpotentials from the GITT voltage curve agree with the C/20 galvanostatic voltage curve.

The last few steps of the GITT charge yield very little capacity. Ultimately, the charge capacity does not exceed the theoretical capacity calculated from the Ni<sup>2+/4+</sup> redox couple although there is plenty of lithium remaining in LNSO-15 to extract. This is in contrast to other lithium-excess materials which continue to charge along a 4.5 V plateau beyond their theoretical capacities until all lithium is removed.<sup>2,20</sup>

The rate tests and GITT measurement suggest that the 4.45 V plateau is due to a kinetically limited process and that higher capacities can be obtained if we bypass this process. Indeed, we show that the 4.45 V plateau can be bypassed until the first slow charge of the cell. Figure 4a shows the voltage

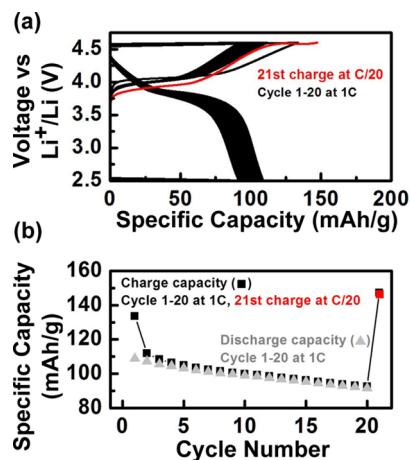


**Figure 4.** (a) Galvanostatic cycling of LNSO-15 at 1C for the first 20 cycles. On the 21st cycle, the charge current is reduced to C/20, and a second plateau is observed at 4.6 V. The second plateau is observed only on the first slow charge, regardless of previous time spent at high voltages during cycling. (b) Charge capacity of cycles 1–20 at 1C and cycle 21 at C/20 and discharge capacity of cycles 1–20 at 1C.

curves of a cell where the first 20 cycles are at 1C, but the 21st charge has been slowed to C/20. While the first 20 cycles bypass the slow process, the characteristic 4.45 V plateau appears on the 21st charge, although its voltage is slightly pushed up. Thus, prior time spent at high voltage does not affect the appearance of the 4.45 V plateau. A cell charged at C/20 in its first cycle spends equivalent time at high voltages as a cell cycled 20 times at 1C. The plateau still appears on the

first slow charge of the cell. This phenomena can be seen more clearly in Figure 4b, where the specific charge and discharge capacities are plotted as a function of cycle number, and we observe a spike in charge capacity on the slow, 21st charge. Due to cell variability in high rate testing, the discharge capacities in Figure 4 are lower than in Figure 2.

**Characterization of Active Redox Processes.** The rate-dependent voltage curves of LNSO-15 motivate further characterization on the redox processes active at fast and slow rates. We first investigate the redox activity of nickel with X-ray absorption near edge structure (XANES) and look at the nickel K-edge position to determine its oxidation state. *Ex situ* XANES measurements were made for three LNSO-15 samples: pristine, charged to 4.6 V at 1C, and charged to 4.6 V at C/20. Reference measurements for the edge positions of Ni<sup>2+</sup> and Ni<sup>3+</sup> are marked by LNSO-0 and NaNiO<sub>2</sub>, respectively. XANES reference measurements were also taken on NiO (not shown) to confirm the Ni<sup>2+</sup> valence state of LNSO-0. Figure 5a shows the

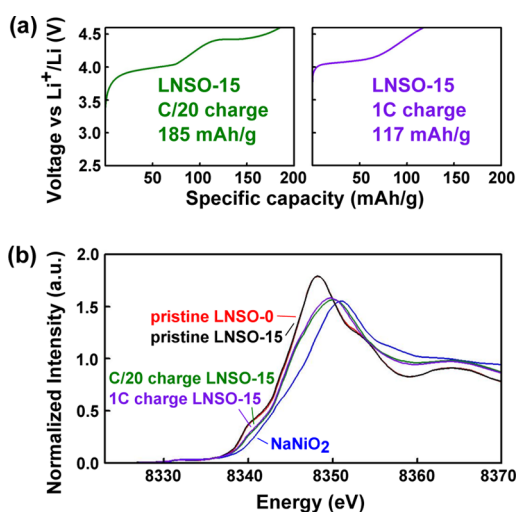


**Figure 5.** (a) Voltage curves and (b) *ex situ* XANES spectra of the nickel K-edge for pristine and fully charged LNSO-15 samples charged at 1C and C/20. Reference edge positions for Ni<sup>2+</sup> and Ni<sup>3+</sup> are given by LNSO-0 and NaNiO<sub>2</sub>. The edge positions of the charged LNSO-15 samples show that, for both rates, nickel is oxidized to a similar valence state between Ni<sup>2+</sup> and Ni<sup>3+</sup>.

voltage curves of the *ex situ* charged LNSO-15 samples, and Figure 5b shows the nickel K-edge positions from XANES of the reference samples and LNSO-15 samples.

*Ex situ* XANES confirms that pristine LNSO-15 contains Ni<sup>2+</sup>; the edge position aligns well with the LNSO-0 reference. Upon charging, we expect nickel to oxidize. The 1C sample reaches 117 mAh/g at the end of charge, and the C/20 sample reaches 185 mAh/g. Both charge capacities fall between the one-electron and two-electron theoretical capacities of 109.5 and 219 mAh/g, calculated from Ni<sup>2+/3+</sup> and Ni<sup>2+/4+</sup>, respectively. Surprisingly, despite a difference of 70 mAh/g and both experimental capacities exceeding the one-electron theoretical capacity, the nickel K-edge positions are nearly identical and lie between the Ni<sup>2+</sup> and Ni<sup>3+</sup> standards. We cannot say what the exact valence of Ni is, but it clearly does not exceed Ni<sup>3+</sup>.

To support the XANES measurements, we also characterize the nickel valence state using electron energy loss spectroscopy (EELS). In EELS measurements, the L3/L2 ratio of the transition metal edges is used as a measure of the oxidation state

of the metal.<sup>21</sup> *Ex situ* EELS measurements on the nickel K-edge were made for pristine LNSO-15, LNSO-15 charged to 69 mAh/g at 1C and C/20 through the end of the first plateau, and LNSO-15 fully charged to 4.6 V at 1C (138 mAh/g) and C/20 (158 mAh/g). The voltage curves for the half-charged and fully charged LNSO-15 samples are shown in Figure 6a.

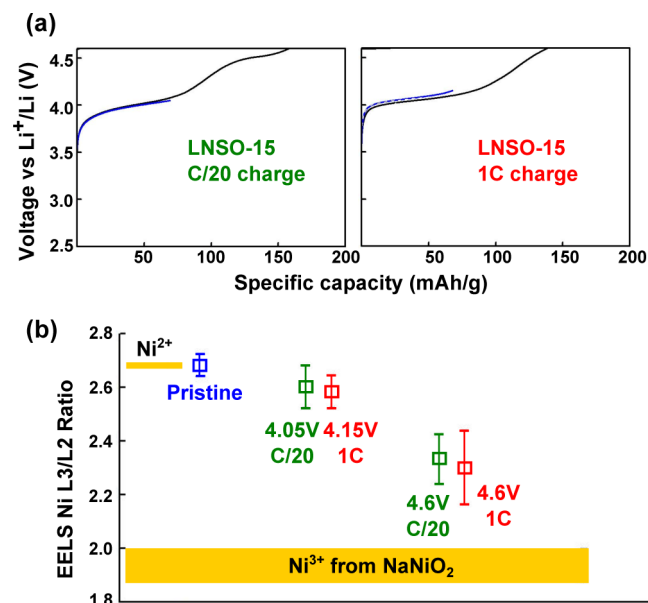


**Figure 6.** (a) Voltage curves and (b) L3/L2 ratio of the nickel K-edge obtained from *ex situ* EELS measurements for pristine, half-charged, and fully charged LNSO-15 samples charged at 1C and C/20. Reference L3/L2 ratios for Ni<sup>2+</sup> and Ni<sup>3+</sup> are represented by horizontal bars. At the end of charge for both rates, nickel is oxidized to a similar valence state between Ni<sup>2+</sup> and Ni<sup>3+</sup>.

There is some variability in the charge capacity between *ex situ* samples used for XANES and *ex situ* samples used for EELS measurements, but the shape of the voltage curves are consistent between the 1C samples and C/20 samples.

Figure 6b plots the L3/L2 ratio of the Ni K-edge for the LNSO-15 samples versus reference samples. From XANES, we know that pristine LNSO-15 contains Ni<sup>2+</sup>; hence, a thin horizontal bar is drawn next to pristine LNSO-15 to represent the Ni<sup>2+</sup> reference. The wider horizontal bar represents the Ni<sup>3+</sup> reference, obtained from EELS measurements on NaNiO<sub>2</sub>. The L3/L2 ratios obtained for the charged LNSO-15 samples are given with error bars. The EELS measurements agree with the findings from XANES: Ni oxidizes to similar states at half charge and full charge regardless of C-rate but does not oxidize past Ni<sup>3+</sup>.

Plateaus at 4.5 V in many lithium-excess materials have been extensively characterized and attributed to a range of phenomena including spinel formation and oxygen loss.<sup>13,22–27</sup> On the basis of these prior studies, we hypothesized that the 4.45 V plateau in lithium-excess LNSO materials may be due to oxygen loss, although the plateau length is much shorter than in other materials. Lu and Dahn<sup>28</sup> were one of the first to correlate changes in structure with oxygen loss phenomena, studying lithium-excess Ni–Mn oxides with *in situ* X-ray diffraction (XRD). From diffraction patterns taken along an electrochemical curve, changes in lattice parameters can be correlated to voltage curve features. Some evidence for transition metal undercoordination was also seen in prior extended X-ray absorption fine structure (EXAFS) studies.<sup>29</sup>

The top graph in Figure 7a shows the first charge voltage curve of LNSO-15 obtained during *in situ* XRD at C/20. Black

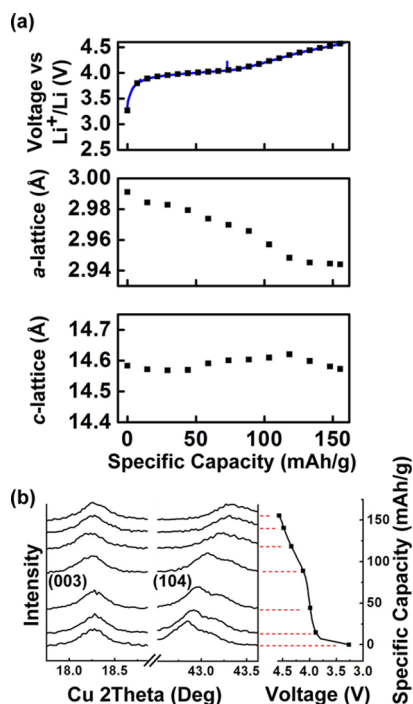


**Figure 7.** *In situ* XRD of LNSO-15 at C/20. (a) First charge voltage curve, *a*-lattice parameter evolution, and *c*-lattice parameter evolution. (b) (003) and (104) peak evolution over the first charge.

dots along the voltage curve mark the points where XRD patterns were obtained. The middle and bottom graphs in Figure 7a show *a*-lattice and *c*-lattice parameter evolution. Figure 7b shows the evolution of the (003) and (104) peaks during first charge.

The shifting (003) and (104) peaks, characteristic peaks of the layered structure, show that LNSO-15 evolves as a single phase in the layered structure and does not fully convert to a disordered rocksalt upon charge. Indeed, after ten cycles at C/20 (not shown), LNSO-15 remains predominantly layered although increased mixing between the lithium and transition metal layers does occur. There is no peak splitting observed, in contrast to observations by Koga et al.<sup>30,31</sup> made on lithium-excess  $\text{Li}_{1.20}\text{Mn}_{0.54}\text{Co}_{0.13}\text{Ni}_{0.13}\text{O}_2$ . The *c*-lattice parameter of LNSO-15 initially expands due to increased repulsion between oxygen atoms surrounding the vacated lithium layer and then contracts at higher levels of delithiation. The *a*-lattice parameter decreases linearly in the first part of the charge as a result of the oxidation of the transition metal, which reduces its radius.<sup>28,32</sup> At the end of the charge along the 4.45 V plateau, the *a*-lattice parameter is constant. The changes in the *c*- and *a*-lattice parameters result in a 4% volume decrease over the first charge.

Online electrochemical mass spectroscopy (OEMS) measurements are conducted for two LNSO materials: LNSO-0, which does not contain lithium excess and does not show a 4.45 V plateau, and LNSO-15, the 15% lithium-excess material that shows the 4.45 V plateau. Working under the hypothesis that the 4.45 V plateau is correlated to oxygen loss, the LNSO-0 sample acts as a control sample that should not show oxygen loss.

Figure 8 shows the first charge voltage curves of LNSO-0 and LNSO-15, obtained with *in situ* OEMS, and the corresponding

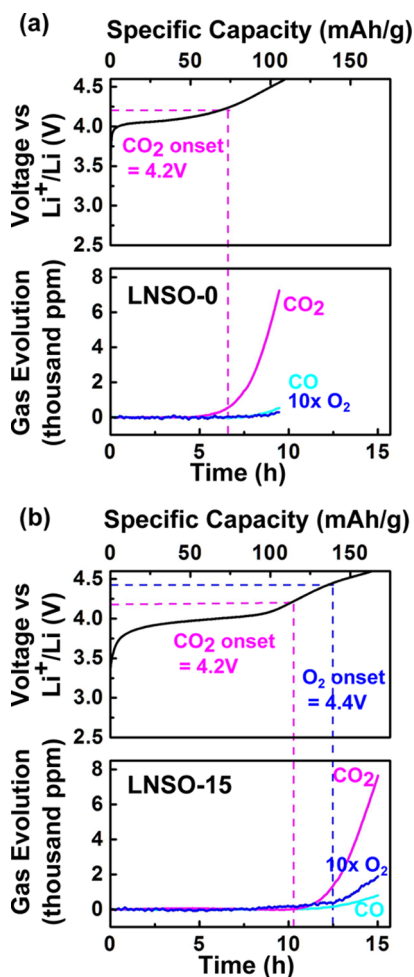


**Figure 8.** Voltage curves and gas evolution measurements from *in situ* OEMS of (a) LNSO-0 and (b) LNSO-15, both charged at C/20. Only LNSO-15 shows oxygen evolution starting at 4.4 V. The O<sub>2</sub> signal is multiplied by 10X to be plotted on the same scale as the CO<sub>2</sub> and CO signals.

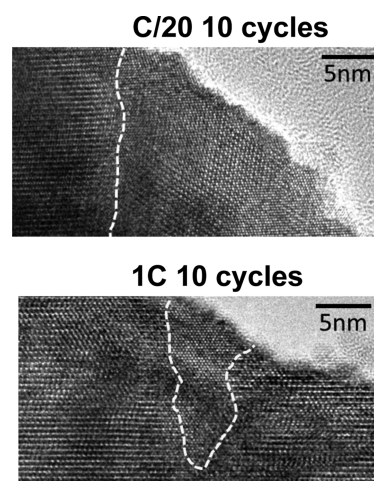


**Figure 9.** HRTEM comparing bulk layered structures to transformed surface structures of LNSO-15 after cycling at 1C and C/20.

concentration of gas species in the cell in thousands of ppm. The ppm quantity can be converted to moles using the volume of the OEMS cell. In both LNSO-0 and LNSO-15, CO<sub>2</sub> evolution begins at 4.2 V but only in LNSO-15 do we also

see an O<sub>2</sub> signal at the start of the 4.45 V plateau. The O<sub>2</sub> signal is multiplied by 10× to be plotted on the same scale as the CO<sub>2</sub> signal and, while small, the O<sub>2</sub> signal is significant.

Finally, HRTEM images were taken to highlight differences in surface evolution after cycling. Figure 9 shows HRTEM images of LNSO-15 cycled at C/20 and 1C. The white dashed lines mark the boundary where the surface regions have undergone structural modification from the layered structure to more three-dimensional like structures. The modified surface phase extends over a significantly larger area for the sample cycled at lower rate.

## DISCUSSION

The electrochemical performance of LNSO-15 inspires two questions. First, how can a material show higher discharge capacities at higher rates? Second, how can a sample cycled at high rate, presumably deviating more from equilibrium, show lower voltages at any point of charge than a sample cycled at low rate? The different voltage curves accessed at slow and fast rates can only be explained by the LNSO-15 material traversing different pathways at different rates. In particular, the electrochemical data suggests that the improved rate performance of LNSO-15 at higher rates is linked to the bypass of the 4.45 V plateau.

From electrochemical tests, we know that the 4.45 V plateau appears with increasing lithium content in the LNSO chemistry. Similar analogies in the literature can be found in other chemistries where a lithium-excess compound shows a plateau at ~4.5 V, but its stoichiometric equivalent does not.<sup>20,28</sup> We also know that LNSO-15's 4.45 V plateau is a kinetically limited process that leads to irreversible capacity loss on discharge. Higher capacities can be obtained if we bypass this 4.45 V process, and the process can indeed be bypassed until the first slow charge of the cell. To determine what occurs along the 4.45 V plateau and what redox processes are active at different rates, we step through evidence for all possible redox reactions in LNSO-15: nickel redox, oxygen loss, and oxygen redox.

On the basis of nickel valence measurements, topotactic lithium removal with nickel redox activity cannot explain the rate-dependent voltage curves of LNSO-15. *Ex situ* XANES and EELS measurements on nickel taken at half charge and full charge at 1C and C/20 both indicate that, although the 1C and C/20 samples achieve different capacities at the end of charge and show different voltage curve features, nickel is oxidized to a similar valence state between Ni<sup>2+</sup> and Ni<sup>3+</sup>. The limited oxidation of nickel implies that the Ni<sup>3+/4+</sup> redox couple may not be accessible, contrary to the assumption in our initial material design. We also confirm that nickel is the only redox-active metal in the LNSO system. XANES on the antimony K-edge shows that no changes to antimony are observed in either charged or cycled samples, confirming that Sb<sup>5+</sup> is electrochemically inactive.

Having determined there is no antimony activity and limited nickel oxidation, we consider evidence for oxygen loss. Characterization on the C/20 charge with *in situ* XRD indirectly suggests oxygen loss to occur along the 4.45 V plateau. *In situ* XRD shows the *a*-lattice parameter to decrease linearly at the beginning of charge, corresponding to transition metal oxidation and shrinking ionic radii. Along the 4.45 V plateau, the *a*-lattice parameter is constant, implying there is no longer transition metal oxidation and that capacity instead comes from oxygen loss. To verify these preliminary results, higher quality *in situ* XRD data should be collected at a beamline. Since the

initial study by Lu and Dahn correlating constant *a*-lattice parameter along a 4.5 V plateau with oxygen loss on the first charge,<sup>28</sup> similar observations have been made in other lithium-excess materials.<sup>33</sup>

Direct detection of oxygen gas by electrochemical mass spectrometry is another proven method to characterize oxygen loss.<sup>34–41</sup> At C/20, OEMS shows oxygen evolution in LNSO-15 to correlate with the second plateau starting at 4.4 V. However, unlike previous reports, the O<sub>2</sub> levels are secondary to the CO<sub>2</sub> levels by an order of magnitude. While O<sub>2</sub> evolution cannot account for all the capacity observed along the 4.45 V plateau, the amount is significant enough that it cannot be ignored as an artifact. When considered in the context of first charge oxygen loss in other lithium-excess materials, it is also not surprising that oxygen loss occurs along the 4.45 V plateau in LNSO-15.

The majority of the CO<sub>2</sub> evolution likely results from direct decomposition of the electrolyte, although some contributions to CO<sub>2</sub> and CO may be attributed to evolved oxygen reacting with the electrolyte. This hypothesis is supported by our observation of two distinct voltage thresholds for CO<sub>2</sub> (4.2 V) and O<sub>2</sub> (4.4 V) evolution, as well as significant CO<sub>2</sub> released in LNSO-0, which does not show a 4.45 V plateau. The OEMS measurements on LNSO-0 illustrates that, even in a sample that does not release O<sub>2</sub>, high levels of CO<sub>2</sub> are still released starting at 4.2 V. While this voltage is lower than expected, different chemistries are known to show a range of electrolyte decomposition voltages.<sup>42</sup> Notably, LiNiO<sub>2</sub> has a very low decomposition voltage of 4.2 V.<sup>43</sup>

Unfortunately, due to experimental restrictions, neither *in situ* XRD nor *in situ* OEMS measurements could be conducted at high C-rates for LNSO-15. XRD patterns require 40 min to collect and thus could not take an accurate snapshot of any structure along a 1C voltage curve charging in 1 h. With OEMS, the high loading of the cathode films required for the OEMS experiment precluded high rate tests from being meaningful in analysis, as significant polarization on the materials resulted in very low capacities. Further studies are needed to investigate oxygen loss at high C-rates. Simply cycling to higher potentials may reveal if the oxygen loss plateau is pushed to a higher potential at higher rates due to diffusion limitations. However, surface changes in cycled samples do suggest that a limited amount of oxygen loss may be occurring at high C-rates, even if the 4.45 V plateau is not observed. The HRTEM images in Figure 9 show that the surface structure has transformed in both the C/20 and 1C cycled samples from the original layered features into more 3-dimensional like structures, possibly by transition metal migration.<sup>25</sup> Structure reorganization is known to accompany oxygen loss, which we presume to occur only from the surface.<sup>22,30,31,39,44</sup>

Having shown there is some nickel oxidation and some oxygen loss in LNSO-15, we now quantify each component's contribution to observed capacity. In the LNSO system, only nickel and oxygen evolve with delithiation. Nickel shows limited oxidation to somewhere between Ni<sup>2+</sup> and Ni<sup>3+</sup>. The theoretical capacity of LNSO-15 calculated from the Ni<sup>2+/3+</sup> redox couple is 109.5 mAh/g. Therefore, on the basis of the observed oxidation state of nickel in LNSO-15, nickel can only account for less than 109.5 mAh/g of reversible capacity.

From *ex situ* XANES, we conclude that antimony has no contributions to observable capacity. It is an electrochemically inactive spectator, remaining Sb<sup>5+</sup> throughout cycling. Antimony's inactivity explains why we observe irreversible capacity

loss after oxygen loss along the 4.45 V plateau. Because antimony cannot be reduced, we cannot activate a second transition metal upon discharge after oxygen loss. This is in contrast to lithium-excess manganese-containing materials, which show manganese reduction on discharge after oxygen evolves on the first charge.<sup>5,45</sup>

We now consider the contribution to capacity from oxygen loss. By the end of charge, LNSO-15 releases 150 ppm of O<sub>2</sub>, which is equivalent to  $5.8 \times 10^{-8}$  moles (in a 9.5 mL cell volume). The detected amount of O<sub>2</sub> is approximately forty times less than the expected amount of evolved O<sub>2</sub>, which is estimated to be  $2.5 \times 10^{-6}$  moles. This estimate is calculated using the active material loading ( $6.9 \times 10^{-3}$  g LNSO-15) and molecular weight of LNSO-15 (113.8 g/mol). Since one mole of LNSO-15 corresponds to one mole of O<sub>2</sub>, the total amount of O<sub>2</sub> in the electrode is  $6.1 \times 10^{-5}$  moles. However, not all O<sub>2</sub> can evolve.

From the HRTEM (Figure 9), we observe that only the outer regions of the LNSO-15 particles undergo structural modification. Thus, our first assumption is that oxygen is released only at the outer 10 nm of the 100 nm diameter particles,<sup>16</sup> which makes up a volume fraction of 0.27. Our second assumption is that the material undergoes some densification, where the amount of oxygen released from the outer shell is roughly equal to the lithium-excess content of 15%.<sup>28</sup> Multiplying  $6.1 \times 10^{-5}$  moles O<sub>2</sub>  $\times$  0.27  $\times$  0.15 gives our estimation of  $2.5 \times 10^{-6}$  moles of O<sub>2</sub> evolved. Comparing this estimation to the experimentally detected moles of O<sub>2</sub>, there is a factor of forty between theory and experiment. The lower quantity of evolved O<sub>2</sub> may be explained by the reaction of evolved lattice oxygen with electrolyte. Previous studies have shown that cyclic carbonates are easily attacked by oxygen anions or oxygen radicals, leading to CO<sub>2</sub> formation.<sup>40,46</sup> The corresponding oxygen fraction would then be missing in the oxygen balance and cannot be differentiated from the CO<sub>2</sub> evolved from electrolyte decomposition. Even accounting for both scenarios to lower the detected amount of O<sub>2</sub>, oxygen loss can only account for a small part of capacity.

Having quantified nickel, antimony, and oxygen loss capacity contributions, significant capacity remains unaccounted for. To summarize the known redox activities in LNSO-15: (1) Nickel shows limited oxidation between Ni<sup>2+</sup> and Ni<sup>3+</sup> when charging to 4.6 V at both slow and fast rates. (2) Antimony is inactive and has no contributions to capacity. (3) Oxygen loss occurs on the first slow charge starting at 4.4 V but cannot account for all remaining capacity. We now consider the only remaining redox process that could contribute to capacity: oxygen redox from O<sup>2-</sup> to O<sup>-</sup>. Oxygen redox activity has been shown to be facilitated by Li excess, as the occurrence of Li–O–Li configurations creates labile oxygen orbitals which are more easily oxidized than the oxygen orbitals which are covalently bonded to a transition metal.<sup>47</sup>

While experiments remain to be completed to confirm oxygen redox and a reliable means of calculating the oxygen redox voltage has yet to be established, we believe that oxidation of O<sup>2-</sup> to O<sup>-</sup> can explain the remaining capacity observed in LNSO-15. Given the observation of oxygen loss at 4.4 V, it is likely that oxygen redox occurs within the electrochemical cycling window at a similar voltage to oxygen loss or at a lower voltage concurrently with nickel oxidation. Additionally, reversible oxygen redox has been suggested in other lithium-excess materials as a mechanism with good Coulombic efficiency.<sup>31,37,41,47–50</sup> Thus, we propose the following redox

sequence for charge: nickel is oxidized first from Ni<sup>2+</sup> to Ni<sup>3+</sup>, followed by oxygen oxidation, which occurs as both oxygen loss on the surface and oxygen redox in the bulk. Given limitations of *in situ* techniques, oxygen loss is only confirmed at slow rates but likely occurs to a lesser extent at fast rates.

Having shed light on the active redox processes in LNSO-15, we attempt to answer the questions posed at the beginning of the discussion. Because similar oxidation processes are observed at slow and fast rate, the rate-dependent voltage curves cannot simply be explained by competition between different redox processes. Redox processes cannot explain why LNSO-15's voltage curves diverge at fast and slow rates, resulting in the bypass of the 4.45 V plateau and higher discharge capacities at faster rates. Such divergent behavior can only be explained by a change in the material that is rate dependent. Comparing the fast and slow rate voltage curves indicates that, at slow rate, a critical change in the material occurs by midcharge after the 4 V plateau. It is important to note here that oxygen loss, while observed at slow rates, occurs *after* this critical point and thus cannot be the cause of the divergent rate behavior.

To reconcile the observed electrochemical behavior, we propose that *nickel migration* is the rate-dependent critical process and dictates the reversible capacity of LNSO-15 in the following manner:

1. In the initial charge along the 4 V plateau, delithiation is accompanied by oxidation of nickel ions in the transition metal layer from Ni<sup>2+</sup> to Ni<sup>3+</sup>.
  - (a) With slow charge, an increasing number of lithium site vacancies and additional time for migration allow some Ni<sup>2+</sup> ions to migrate from the transition metal layer to stabilize the delithiated structure. Ni<sup>2+</sup> migrates either to tetrahedral sites or to octahedral sites in the lithium layer to lower its site energy.
  - (b) With fast charge, few Ni<sup>2+</sup> ions migrate from the transition metal layer, and the material remains well-layered.
2. In the second half of charge from  $\sim$ 4.1 to 4.6 V, nickel oxidation from Ni<sup>2+</sup> to Ni<sup>3+</sup> occurs concurrent with oxygen oxidation in the form of oxygen loss at the surface (O<sup>2-</sup>  $\rightarrow$  O<sub>2</sub>(g)) and oxygen redox in the bulk (O<sup>2-</sup>  $\rightarrow$  O<sup>-</sup>).
  - (a) With slow charge, the 4.45 V plateau accompanies oxidation of the *migrated* Ni<sup>2+</sup>. Once oxidized to Ni<sup>3+</sup>, nickel will prefer octahedral sites in the lithium layer, and further migration becomes energetically unfavorable. It is well-known that size effects make Ni<sup>3+</sup> in the lithium layer much more difficult to oxidize.<sup>51</sup>
  - (b) With fast charge, because little Ni<sup>2+</sup> migration has occurred, topotactic delithiation continues with oxidation of nickel ions in the transition metal layer, hence a longer 4 V plateau. An oxygen loss plateau may not appear until higher potentials due to diffusion limitations.
3. On discharge, lithiation is accompanied by reduction of Ni<sup>3+</sup> to Ni<sup>2+</sup> and reduction of oxygen from O<sup>-</sup> to O<sup>2-</sup>.
  - (a) Following a slow charge, a significant number of Ni<sup>3+</sup> ions becomes “stuck” in the migrated sites. Any migrated Ni<sup>3+</sup> cannot move back to the transition metal layer until reduced to Ni<sup>2+</sup>. At the same

time, not all migrated  $\text{Ni}^{3+}$  can be reduced, as the migrated ions block all neighboring vacant lithium sites for intercalation.

- (b) Following a fast charge, because little nickel migration has occurred, more lithium can be reintercalated as all sites are available, yielding higher discharge capacities.

Although further experiments are needed to confirm nickel migration in LNSO-15,<sup>52</sup>  $\text{Ni}^{2+}$  migration has been suggested on theoretical grounds,<sup>53</sup> and nickel-containing cathode materials, including  $\text{LiNi}_{2/3}\text{Sb}_{1/3}\text{O}_2$ ,<sup>54</sup> are known to be prone to nickel migration and cation mixing.<sup>28,52,55–58</sup> Having thoroughly characterized redox activity at slow and fast rate, we believe that nickel migration can explain the anomalous rate behavior of LNSO-15 and is substantiated by the literature.

We first consider nickel's migration tendencies and site preferences.  $\text{Ni}^{2+}$  has low migration barriers due to its low valence state and can occupy both tetrahedral and octahedral sites in close-packed crystal structures.<sup>52–54,59</sup> In contrast,  $\text{Ni}^{3+}$  and  $\text{Ni}^{4+}$  have much higher migration barriers<sup>60</sup> and only prefer to occupy octahedral sites.<sup>52,61</sup>

Pristine LNSO-15 contains only  $\text{Ni}^{2+}$ . Until appreciable delithiation occurs, few vacancies on the lithium sites may be available to facilitate nickel migration. Thus, the critical point where fast and slow voltage curves diverge occurs after LNSO-15 has traversed the 4 V plateau and  $\sim 0.3$  Li has been extracted. At this critical point, halfway through charge, LNSO-15 contains both lithium vacancies and  $\text{Ni}^{2+}$  ions. At high rate, nickel migration occurs at a slower rate than delithiation; thus,  $\text{Ni}^{2+}$  largely remains in octahedral sites in the transition metal layer and is oxidized to  $\text{Ni}^{3+}$  before it has a chance to migrate. In contrast, gradual delithiation at slow rate allows sufficient time for  $\text{Ni}^{2+}$  migration to either tetrahedral sites or vacant octahedral sites in the lithium layer. If  $\text{Ni}^{2+}$  goes to tetrahedral sites, it will later move to octahedral sites in the lithium layer upon oxidation to  $\text{Ni}^{3+}$ . If  $\text{Ni}^{2+}$  migrates directly to octahedral sites in the lithium layer, it will stay in these sites upon oxidation to  $\text{Ni}^{3+}$ .

At the end of charge,  $\text{Ni}^{3+}$  ions are stable in octahedral sites in the lithium layer. If these migrated  $\text{Ni}^{3+}$  do not move back to their original positions in the transition metal layer, then the irreversible capacity loss observed after first charge can be explained as a combined effect of oxygen loss and site availability.<sup>24,25,51,62,63</sup> When LNSO-15 evolves oxygen upon charge, lithium ions extracted with oxygen evolution cannot be reinserted upon discharge, as  $\text{Sb}^{5+}$  is not redox active. Additionally, fewer sites for lithium are available for lithium reinsertion on discharge if  $\text{Ni}^{3+}$  remains in the lithium layer, as it blocks all neighboring vacant lithium sites.<sup>64</sup> The detrimental effects of nickel migration are pronounced at slow rates, especially in the first slow charge when the majority of the nickel migration occurs. The reduction of site availability from nickel migration also explains why cycling at slow rates (more nickel migration) leads to larger capacity fade, while cycling at fast rates (less nickel migration) has better capacity retention.

## CONCLUSION

The lithium-excess LNSO materials containing 0–15% lithium excess were studied as a function of lithium content and rate. At slow C-rates, we observe improved cyclability with increasing lithium content but also irreversible capacity loss after the first cycle correlating with a plateau at 4.45 V. The length of the

4.45 V plateau scales with increasing lithium content. For the LNSO-15 sample, faster C-rates lead to the disappearance of the 4.45 V plateau, as well as unexpectedly higher discharge capacities.

Through a number of characterization techniques, we set out to understand what phenomena are responsible for different voltage curve features at slow and fast rates and how higher discharge capacities can be achieved at faster C-rates. Using *ex situ* XANES and EELS, we confirm that nickel is oxidized to a similar valence state at the end of the charge but only to somewhere between  $\text{Ni}^{2+}$  and  $\text{Ni}^{3+}$ . From *in situ* XRD and OEMS, we determine that nickel oxidation occurs along the first 4 V plateau, followed by oxygen loss along the second 4.45 V plateau. The case for oxygen loss is further supported by surface structure evolution observed in HRTEM.

The experimental capacity cannot be fully explained by the limited nickel oxidation and oxygen loss. Thus, we propose that the final redox process that is active in the LNSO-15 system may be reversible oxygen redox from  $\text{O}^{2-}$  to  $\text{O}^-$ . Additionally, we suggest that the degree of nickel migration in LNSO-15 dictates the reversible capacity in the material. When significant nickel migration occurs to the lithium layer during slow charge, the surrounding vacant lithium sites become unavailable on discharge, thus reducing the discharge capacity. In contrast, because nickel migration is minimized in fast charge, higher discharge capacities can be attained at higher C-rates.

## ASSOCIATED CONTENT

### Supporting Information

The Supporting Information is available free of charge on the ACS Publications website at DOI: 10.1021/acs.chemmater.6b04691.

ICP elemental analysis, full *in situ* XRD scans, and *ex situ* XRD after cycling (PDF)

## AUTHOR INFORMATION

### Corresponding Author

\*E-mail: gceder@berkeley.edu.

### ORCID

Nancy Twu: 0000-0002-1433-5229

### Notes

The authors declare no competing financial interest.

## ACKNOWLEDGMENTS

N.T. thanks Alexander Urban, Jinhyuk Lee, Dong-Hwa Seo, and Rahul Malik for helpful discussions. Work by N.T., X.L., and H.C. was supported by Robert Bosch Corporation and Umicore. M.M. and C.M. would like to acknowledge funding by BASF SE and BMW AG, respectively. This work made use of MRSEC Shared Experimental Facilities at MIT, supported by the National Science Foundation under award # DMR-08-19762. Research at sector 20-BM at the Advanced Photon Source was supported by U.S. DOE under Contract No. DE-AC02-06CH11357.

## REFERENCES

- (1) Yu, H.; Zhou, H. High-Energy Cathode Materials ( $\text{Li}_2\text{MnO}_3\text{-LiMO}_2$ ) for Lithium-Ion Batteries. *J. Phys. Chem. Lett.* **2013**, *4*, 1268–1280.
- (2) Yabuuchi, N.; Takeuchi, M.; Endo, D.; Ozaki, T.; Inamasu, T.; Son, J.-Y.; Cui, Y.-T.; Oji, H.; Komaba, S. Synthesis, Electrochemical Properties, and Reaction Mechanisms of New Lithium-Excess

Transition Metal Oxides with Cation Disordered Rock-Salt-Type Structure. Abstract #874; 224th ECS Meeting, San Francisco, California, October 27 to November 1, 2013.

(3) Lee, J.; Urban, A.; Li, X.; Su, D.; Hautier, G.; Ceder, G. Unlocking the Potential of Cation-Disordered Oxides for Rechargeable Lithium Batteries. *Science* **2014**, *343*, 519–522.

(4) Johnson, C. S.; Kim, J.-S.; Lefief, C.; Li, N.; Vaughey, J. T.; Thackeray, M. M. The significance of the  $\text{Li}_2\text{MnO}_3$  component in 'composite'  $x\text{Li}_2\text{MnO}_3$   $(1-x)\text{LiMn}_{0.5}\text{Ni}_{0.5}\text{O}_2$  electrodes. *Electrochem. Commun.* **2004**, *6*, 1085–1091.

(5) Yabuuchi, N.; Yoshii, K.; Myung, S.-T.; Nakai, I.; Komaba, S. Detailed studies of a high-capacity electrode material for rechargeable batteries,  $\text{Li}_2\text{MnO}_3$ - $\text{LiCo}_{1/3}\text{Ni}_{1/3}\text{Mn}_{1/3}\text{O}_2$ . *J. Am. Chem. Soc.* **2011**, *133*, 4404–4419.

(6) Thackeray, M. M.; Johnson, C. S.; Vaughey, J. T.; Li, N.; Hackney, S. A. Advances in manganese-oxide 'composite' electrodes for lithium-ion batteries. *J. Mater. Chem.* **2005**, *15*, 2257–2267.

(7) Thackeray, M. M.; Kang, S.-H.; Johnson, C. S.; Vaughey, J. T.; Benedek, R.; Hackney, S. A.  $\text{Li}_2\text{MnO}_3$ -stabilized  $\text{LiMO}_2$  ( $M = \text{Mn}, \text{Ni}, \text{Co}$ ) electrodes for lithium-ion batteries. *J. Mater. Chem.* **2007**, *17*, 3112–3125.

(8) Yu, H.; Wang, Y.; Asakura, D.; Hosono, E.; Zhang, T.; Zhou, H. Electrochemical kinetics of the  $0.5\text{Li}_2\text{MnO}_3$   $0.5\text{LiMn}_{0.42}\text{Ni}_{0.42}\text{Co}_{0.16}\text{O}_2$  'composite' layered cathode material for lithium-ion batteries. *RSC Adv.* **2012**, *2*, 8797–8807.

(9) van Bommel, A.; Dahn, J. R. Kinetics Study of the High Potential Range of Lithium-Rich Transition-Metal Oxides for Lithium-Ion Batteries by Electrochemical Methods. *Electrochem. Solid-State Lett.* **2010**, *13*, A62–A64.

(10) Kang, S.-H.; Thackeray, M. M. Enhancing the rate capability of high capacity  $x\text{Li}_2\text{MnO}_3$   $(1-x)\text{LiMO}_2$  ( $M = \text{Mn}, \text{Ni}, \text{Co}$ ) electrodes by Li-Ni-PO<sub>4</sub> treatment. *Electrochem. Commun.* **2009**, *11*, 748–751.

(11) Yu, X.; Lyu, Y.; Gu, L.; Wu, H.; Bak, S.-M.; Zhou, Y.; Amine, K.; Ehrlich, S. N.; Li, H.; Nam, K.-W.; Yang, X.-Q. Understanding the Rate Capability of High-Energy-Density Li-Rich Layered  $\text{Li}_{1.2}\text{Ni}_{0.15}\text{Co}_{0.1}\text{Mn}_{0.55}\text{O}_2$  Cathode Materials. *Adv. Energy Mater.* **2014**, *4*, 1300950.

(12) Zheng, S.; Huang, R.; Makimura, Y.; Ukyo, Y.; Fisher, C. A. J.; Hirayama, T.; Ikuhara, Y. Microstructural Changes in  $\text{Li-Ni}_{0.8}\text{Co}_{0.15}\text{Al}_{0.05}\text{O}_2$  Positive Electrode Material during the First Cycle. *J. Electrochem. Soc.* **2011**, *158*, A357–A362.

(13) Xu, B.; Fell, C. R.; Chi, M.; Meng, Y. S. Identifying surface structural changes in layered Li-excess nickel manganese oxides in high voltage lithium ion batteries: A joint experimental and theoretical study. *Energy Environ. Sci.* **2011**, *4*, 2223–2233.

(14) Boulineau, A.; Simonin, L.; Colin, J.-F.; Bourbon, C.; Patoux, S. First evidence of manganese-nickel segregation and densification upon cycling in Li-rich layered oxides for lithium batteries. *Nano Lett.* **2013**, *13*, 3857–3863.

(15) Urban, A.; Lee, J.; Ceder, G. The Configurational Space of Rocksalt-Type Oxides for High-Capacity Lithium Battery Electrodes. *Adv. Energy Mater.* **2014**, *4*, 1400478.

(16) Twu, N.; Li, X.; Urban, A.; Balasubramanian, M.; Lee, J.; Liu, L.; Ceder, G. Designing new lithium-excess cathode materials from percolation theory: Nanohighways in  $\text{Li}_x\text{Ni}_{2-4x/3}\text{Sb}_{x/3}\text{O}_2$ . *Nano Lett.* **2015**, *15*, 596–602.

(17) Tsiouvaras, N.; Meini, S.; Buchberger, I.; Gasteiger, H. A. A Novel On-Line Mass Spectrometer Design for the Study of Multiple Charging Cycles of a Li-O<sub>2</sub> Battery. *J. Electrochem. Soc.* **2013**, *160*, A471–A477.

(18) Meini, S.; Piana, M.; Tsiouvaras, N.; Garsuch, A.; Gasteiger, H. A. The Effect of Water on the Discharge Capacity of a Non-Catalyzed Carbon Cathode for Li-O<sub>2</sub> Batteries. *Electrochem. Solid-State Lett.* **2012**, *15*, A45–A48.

(19) Metzger, M.; Marino, C.; Sicklinger, J.; Haering, D.; Gasteiger, H. A. Anodic Oxidation of Conductive Carbon and Ethylene Carbonate in High-Voltage Li-Ion Batteries Quantified by On-Line Electrochemical Mass Spectrometry. *J. Electrochem. Soc.* **2015**, *162*, A1123–A1134.

(20) Ohzuku, T.; Nagayama, M.; Tsuji, K.; Ariyoshi, K. High-capacity lithium insertion materials of lithium nickel manganese oxides for advanced lithium-ion batteries: toward rechargeable capacity more than 300 mAhg<sup>-1</sup>. *J. Mater. Chem.* **2011**, *21*, 10179–10188.

(21) Graetz, J.; Ahn, C. C.; Ouyang, H.; Rez, P.; Fultz, B. White lines and *d*-band occupancy for the 3d transition-metal oxides and lithium transition-metal oxides. *Phys. Rev. B: Condens. Matter Mater. Phys.* **2004**, *69*, 235103.

(22) Tran, N.; Croguennec, L.; Ménétrier, M.; Weill, F.; Biensan, P.; Jordy, C.; Delmas, C. Mechanisms Associated with the "Plateau" Observed at High Voltage for the Overlithiated  $\text{Li}_{1.12}(\text{Ni}_{0.425}\text{Mn}_{0.425}\text{Co}_{0.15})_{0.88}\text{O}_2$  System. *Chem. Mater.* **2008**, *20*, 4815–4825.

(23) Ito, A.; Shoda, K.; Sato, Y.; Hatano, M.; Horie, H.; Ohsawa, Y. Direct observation of the partial formation of a framework structure for Li-rich layered cathode material  $\text{Li}[\text{Ni}_{0.17}\text{Li}_{0.2}\text{Co}_{0.07}\text{Mn}_{0.56}]\text{O}_2$  upon the first charge and discharge. *J. Power Sources* **2011**, *196*, 4785–4790.

(24) van Bommel, A.; Krause, L. J.; Dahn, J. R. Investigation of the Irreversible Capacity Loss in the Lithium-Rich Oxide  $\text{Li}[\text{Li}_{1/5}\text{Ni}_{1/5}\text{Mn}_{3/5}]\text{O}_2$ . *J. Electrochem. Soc.* **2011**, *158*, A731–A735.

(25) Jiang, M.; Key, B.; Meng, Y. S.; Grey, C. P. Electrochemical and Structural Study of the Layered, "Li-Excess" Lithium-Ion Battery Electrode Material  $\text{Li}[\text{Li}_{1/9}\text{Ni}_{1/3}\text{Mn}_{5/9}]\text{O}_2$ . *Chem. Mater.* **2009**, *21*, 2733–2745.

(26) Rana, J.; Stan, M.; Kloepsch, R.; Li, J.; Schumacher, G.; Welter, E.; Zizak, I.; Banhart, J.; Winter, M. Structural Changes in  $\text{Li}_2\text{MnO}_3$  Cathode Material for Li-Ion Batteries. *Adv. Energy Mater.* **2014**, *4*, 1300998.

(27) Ates, M. N.; Mukerjee, S.; Abraham, K. M. A Li-Rich Layered Cathode Material with Enhanced Structural Stability and Rate Capability for Li-ion Batteries. *J. Electrochem. Soc.* **2014**, *161*, A355–A363.

(28) Lu, Z.; Dahn, J. R. Understanding the Anomalous Capacity of  $\text{Li}/\text{Li}[\text{Ni}_x\text{Li}_{(1/3-2x/3)}\text{Mn}_{(2/3-x/3)}]\text{O}_2$  Cells Using *In Situ* X-Ray Diffraction and Electrochemical Studies. *J. Electrochem. Soc.* **2002**, *149*, A815–A822.

(29) Balasubramanian, M.; McBreen, J.; Davidson, I. J.; Whitfield, P. S.; Kargina, I. *In Situ* X-Ray Absorption Study of a Layered Manganese-Chromium Oxide-Based Cathode Material. *J. Electrochem. Soc.* **2002**, *149*, A176–A184.

(30) Koga, H.; Croguennec, L.; Ménétrier, M.; Mannesiez, P.; Weill, F.; Delmas, C. Different oxygen redox participation for bulk and surface: A possible global explanation for the cycling mechanism of  $\text{Li}_{1.20}\text{Mn}_{0.54}\text{Co}_{0.13}\text{Ni}_{0.13}\text{O}_2$ . *J. Power Sources* **2013**, *236*, 250–258.

(31) Koga, H.; Croguennec, L.; Ménétrier, M.; Douhil, K.; Belin, S.; Bourgeois, L.; Suard, E.; Weill, F.; Delmas, C. Reversible Oxygen Participation to the Redox Processes Revealed for  $\text{Li}_{1.20}\text{Mn}_{0.54}\text{Co}_{0.13}\text{Ni}_{0.13}\text{O}_2$ . *J. Electrochem. Soc.* **2013**, *160*, A786–A792.

(32) Lu, Z.; Dahn, J. R. *In Situ* and *Ex Situ* XRD Investigation of  $\text{Li}[\text{Cr}_x\text{Li}_{1/3-x/3}\text{Mn}_{2/3-2x/3}]\text{O}_2$  ( $x = 1/3$ ) Cathode Material. *J. Electrochem. Soc.* **2003**, *150*, A1044.

(33) Mohanty, D.; Kalnaus, S.; Meisner, R. A.; Rhodes, K. J.; Li, J.; Payzant, E. A.; Wood, D. L.; Daniel, C. Structural transformation of a lithium-rich  $\text{Li}_{1.2}\text{Co}_{0.1}\text{Mn}_{0.55}\text{Ni}_{0.15}\text{O}_2$  cathode during high voltage cycling resolved by *in situ* X-ray diffraction. *J. Power Sources* **2013**, *229*, 239–248.

(34) Armstrong, A. R.; Holzapfel, M.; Novák, P.; Johnson, C. S.; Kang, S.-H.; Thackeray, M. M.; Bruce, P. G. Demonstrating oxygen loss and associated structural reorganization in the lithium battery cathode  $\text{Li}[\text{Ni}_{0.2}\text{Li}_{0.2}\text{Mn}_{0.6}]\text{O}_2$ . *J. Am. Chem. Soc.* **2006**, *128*, 8694–8698.

(35) La Mantia, F.; Rosciano, F.; Tran, N.; Novák, P. Direct evidence of oxygen evolution from  $\text{Li}_{1+x}(\text{Ni}_{1/3}\text{Mn}_{1/3}\text{Co}_{1/3})_{1-x}\text{O}_2$  at high potentials. *J. Appl. Electrochem.* **2008**, *38*, 893–896.

(36) la Mantia, F.; Rosciano, F.; Tran, N.; Novák, P. Quantification of Oxygen Loss from  $\text{Li}_{1+x}(\text{Ni}_{1/3}\text{Mn}_{1/3}\text{Co}_{1/3})_{1-x}\text{O}_2$  at High Potentials by Differential Electrochemical Mass Spectrometry. *J. Electrochem. Soc.* **2009**, *156*, A823–A827.

(37) Sathiyar, M.; Rouse, G.; Ramesha, K.; Laisa, C. P.; Vezin, H.; Sougrati, M. T.; Doublet, M.-L.; Foix, D.; Gonbeau, D.; Walker, W.;

Prakash, A. S.; ben Hassine, M.; Dupont, L.; Tarascon, J.-M. Reversible anionic redox chemistry in high-capacity layered-oxide electrodes. *Nat. Mater.* **2013**, *12*, 827–835.

(38) Robert, R.; Bunzli, C.; Berg, E. J.; Novák, P. Activation Mechanism of  $\text{LiNi}_{0.80}\text{Co}_{0.15}\text{Al}_{0.05}\text{O}_2$ : Surface and Bulk Operando Electrochemical, DEMS and XRD Analyses. *Chem. Mater.* **2015**, *27*, 526–536.

(39) Hong, J.; Lim, H.-D.; Lee, M.; Kim, S.-W.; Kim, H.; Oh, S.-T.; Chung, G.-C.; Kang, K. Critical Role of Oxygen Evolved from Layered Li-Excess Metal Oxides in Lithium Rechargeable Batteries. *Chem. Mater.* **2012**, *24*, 2692–2697.

(40) Castel, E.; Berg, E. J.; El Kazzi, M.; Novák, P.; Villevieille, C. Differential Electrochemical Mass Spectrometry Study of the Interface of  $x\text{Li}_2\text{MnO}_3$  (1- $x$ ) $\text{LiMO}_2$  (M = Ni, Co, and Mn) Material as Positive Electrode in Li-ion Batteries. *Chem. Mater.* **2014**, *26*, 5051–5057.

(41) Luo, K.; Roberts, M. R.; Hao, R.; Guerrini, N.; Pickup, D. M.; Liu, Y.-S.; Edström, K.; Guo, J.; Chadwick, A. V.; Duda, L. C.; Bruce, P. G. Charge-compensation in 3d-transition-metal-oxide intercalation cathodes through the generation of localized electron holes on oxygen. *Nat. Chem.* **2016**, *8*, 684–691.

(42) Wang, H.; Rus, E. D.; Sakuraba, T.; Kikuchi, J.; Kiya, Y.; Abruña, H. D.  $\text{CO}_2$  and  $\text{O}_2$  Evolution at High Voltage Cathode Materials of Li-ion Batteries: A Differential Electrochemical Spectrometry (DEMS) Study. *Anal. Chem.* **2014**, *86*, 6197–6201.

(43) Imhof, R.; Novák, P. Oxidative Electrolyte Solvent Degradation in Lithium-Ion Batteries: An *In Situ* Differential Electrochemical Mass Spectrometry Investigation. *J. Electrochem. Soc.* **1999**, *146*, 1702–1706.

(44) Genevois, C.; Koga, H.; Croguennec, L.; Ménétrier, M.; Delmas, C.; Weill, F. Insight in the Atomic Structure of Cycled Lithium-Rich Layered Oxide  $\text{Li}_{1.20}\text{Mn}_{0.54}\text{Co}_{0.13}\text{Ni}_{0.13}\text{O}_2$  using HAADF STEM and Electron Nanodiffraction. *J. Phys. Chem. C* **2015**, *119*, 75–83.

(45) Yu, H.; Kim, H.; Wang, Y.; He, P.; Asakura, D.; Nakamura, Y.; Zhou, H. High-energy 'composite' layered manganese-rich cathode materials via controlling  $\text{Li}_2\text{MnO}_3$  phase activation for lithium-ion batteries. *Phys. Chem. Chem. Phys.* **2012**, *14*, 6584–6595.

(46) McCloskey, B. D.; Bethune, D. S.; Shelby, R. M.; Girishkumar, G.; Luntz, A. C. Solvents' Critical Role in Nonaqueous Lithium-Oxygen Battery Electrochemistry. *J. Phys. Chem. Lett.* **2011**, *2*, 1161–1166.

(47) Seo, D.-H.; Lee, J.; Urban, A.; Malik, R.; Kang, S.; Ceder, G. The structural and chemical origin of the oxygen redox activity in layered and cation-disordered Li-excess cathode materials. *Nat. Chem.* **2016**, *8*, 692–697.

(48) Sathiya, M.; Ramesha, K.; Rouse, G.; Foix, D.; Gonbeau, D.; Prakash, A. S.; Doublet, M. L.; Hemalatha, K.; Tarascon, J.-M. High Performance  $\text{Li}_2\text{Ru}_{1-y}\text{MnO}_3$  (0.2 <  $y$  < 0.8) Cathode Materials for Rechargeable Lithium-Ion Batteries: Their Understanding. *Chem. Mater.* **2013**, *25*, 1121–1131.

(49) McCalla, E.; Sougrati, M. T.; Rouse, G.; Jamstorp Berg, E.; Abakumov, A. M.; Recham, N.; Ramesha, K.; Sathiya, M.; Dominko, R.; Van Tendeloo, G.; Novák, P.; Tarascon, J.-M. Understanding the roles of anionic redox and oxygen release during electrochemical cycling of lithium-rich layered  $\text{Li}_4\text{FeSbO}_6$ . *J. Am. Chem. Soc.* **2015**, *137*, 4804–4814.

(50) Lee, J.; Seo, D.-H.; Balasubramanian, M.; Twu, N.; Li, X.; Ceder, G. A new class of high capacity cation-disordered oxides for rechargeable lithium batteries: Li–Ni–Ti–Mo oxides. *Energy Environ. Sci.* **2015**, *8*, 3255–3265.

(51) Peres, J. P.; Delmas, C.; Rougier, A.; Broussely, M.; Pertion, F.; Biensan, P.; Willmann, P. The relationship between the composition of lithium nickel oxide and the loss of reversibility during the first cycle. *J. Phys. Chem. Solids* **1996**, *57*, 1057–1060.

(52) Bréger, J.; Meng, Y. S.; Hinuma, Y.; Kumar, S.; Kang, K.; Shao-Horn, Y.; Ceder, G.; Grey, C. P. Effect of High Voltage on the Structure and Electrochemistry of  $\text{LiN}_{0.5}\text{Mn}_{0.5}\text{O}_2$ : A Joint Experimental and Theoretical Study. *Chem. Mater.* **2006**, *18*, 4768–4781.

(53) Reed, J.; Ceder, G. Role of Electronic Structure in the Susceptibility of Metastable Transition-Metal Oxide Structures to Transformation. *Chem. Rev.* **2004**, *104*, 4513–4534.

(54) Ma, X.; Kang, K.; Ceder, G.; Meng, Y. S. Synthesis and electrochemical properties of layered  $\text{LiNi}_{2/3}\text{Sb}_{1/3}\text{O}_2$ . *J. Power Sources* **2007**, *173*, 550–555.

(55) Dahn, J. R.; Michal, C. A. Structure and electrochemistry of  $\text{Li}_{1-x}\text{NiO}_2$  and a new  $\text{Li}_2\text{NiO}_2$  phase with the  $\text{Ni}(\text{OH})_2$  structure. *Solid State Ionics* **1990**, *44*, 87–97.

(56) Ohzuku, T.; Makimura, Y. Layered Lithium Insertion Material of  $\text{LiNi}_{1/2}\text{Mn}_{1/2}\text{O}_2$ : A Possible Alternative to  $\text{LiCoO}_2$  for Advanced Lithium-Ion Batteries. *Chem. Lett.* **2001**, *30*, 744–745.

(57) Lu, Z.; MacNeil, D. D.; Dahn, J. R. Layered  $\text{Li}[\text{Ni}_x\text{Co}_{1-2x}\text{Mn}_x]\text{O}_2$  Cathode Materials for Lithium-Ion Batteries. *Electrochem. Solid-State Lett.* **2001**, *4*, A200–A203.

(58) Croy, J. R.; Balasubramanian, M.; Kim, D.; Kang, S.-H.; Thackeray, M. M. Designing High-Capacity, Lithium-Ion Cathodes Using X-ray Absorption Spectroscopy. *Chem. Mater.* **2011**, *23*, 5415–5424.

(59) Arachi, Y.; Kobayashi, H.; Emura, S.; Nakata, Y.; Tanaka, M.; Asai, T.; Sakaebe, H.; Tatsumi, K.; Kageyama, H. Li de-intercalation mechanism in  $\text{LiNi}_{0.5}\text{Mn}_{0.5}\text{O}_2$  cathode material for Li-ion batteries. *Solid State Ionics* **2005**, *176*, 895–903.

(60) Kang, K.; Ceder, G. Factors that affect Li mobility in layered lithium transition metal oxides. *Phys. Rev. B: Condens. Matter Mater. Phys.* **2006**, *74*, 094105.

(61) Figgis, B.; Hitchman, M. *Ligand Field Theory and its Applications*; Wiley-VCH: New York, 2000.

(62) Arunkumar, T. A.; Wu, Y.; Manthiram, A. Factors Influencing the Irreversible Oxygen Loss and Reversible Capacity in Layered  $\text{Li}[\text{Li}_{1/3}\text{Mn}_{2/3}]\text{O}_2\text{-Li}[\text{M}]\text{O}_2$  (M =  $\text{Mn}_{0.5-y}\text{Ni}_{0.5-y}\text{Co}_{2y}$  and  $\text{Ni}_{1-y}\text{Co}_y$ ) Solid Solutions. *Chem. Mater.* **2007**, *19*, 3067–3073.

(63) Deng, Z. Q.; Manthiram, A. Influence of Cationic Substitutions on the Oxygen Loss and Reversible Capacity of Lithium-Rich Layered Oxide Cathodes. *J. Phys. Chem. C* **2011**, *115*, 7097–7103.

(64) Rougier, A.; Gravereau, P.; Delmas, C. Optimization of the Composition of the  $\text{Li}_{1-z}\text{Ni}_{1+z}\text{O}_2$  Electrode Materials: Structural, Magnetic, and Electrochemical Studies. *J. Electrochem. Soc.* **1996**, *143*, 1168–1175.